Spin ice physics in a new rare-earth selenide spinel $MgEr_2Se_4$

D. Reig-i-Plessis,[1] S. V. Geldern,[1] A. A. Aczel,[2] and G. J. MacDougall[1,*]

[1] *Department of Physics and Seitz Materials Research Laboratory, University of Illinois at Urbana-Champaign, Urbana, Illinois, 61801, USA*

[2] *Quantum Condensed Matter Division, Oak Ridge National Laboratory, Oak Ridge, Tennessee, 37831, USA*

We present detailed characterization of a novel rare-earth selenide spinel, $MgEr_2Se_4$, which is shown to be one of the only spin ice materials outside the well-studied 227 pyrochlore oxide family. X-ray and neutron diffraction confirm a pyrochlore sublattice of Er^{3+}, and inelastic neutron scattering data reveal that the Er^{3+} spins have a local Ising character. Spin ice signatures are observed in both heat capacity and magnetic diffuse scattering measurements. We argue that the relatively low level of defects in this material may make it an ideal testing ground for monopole predictions.

arXiv:1703.04267v1 [cond-mat.dis-nn] 13 Mar 2017

Rare earth pyrochlores are well known for their variety of exotic ground states facilitated by geometric frustration and non-trivial local crystal electric field (CEF) effects. Prime examples can be found in the $RE_2Ti_2O_7$ family of materials [1, 2], where "spin ice" [3–5], "quantum spin ice" [6–8], spin liquid [9, 10] or "order by disorder" [11, 12] behaviors have been reported, depending on the choice of rare-earth cation[1, 2].

Perhaps mostly widely appreciated of these phases is the spin ice state, which occurs in the materials $Dy_2Ti_2O_7$ and $Ho_2Ti_2O_7$ as a result of local Ising spin symmetry (along local $< 111 >$ directions) and net ferromagnetic spin interactions [13]. A pyrochlore satisfying these two conditions will have the energy minimized when the spins for each tetrahedron are in a 2-in-2-out configuration (shown in the Fig. 1(a) inset). This condition alone is insufficient to select a unique ordered ground state, and the systems instead enter a highly-degenerate frozen state at low temperature with a finite entropy even as $T \to 0$. Residual ("Pauling") entropy [4, 14] and short-range magnetic correlations [15, 16] are considered key experimental signatures of an ice state.

Recent interest in these compounds has been largely driven by a theoretical equivalence between spin flip defects out of a spin ice state and nearly-deconfined pairs of magnetic monopoles [17–19]. Discussions of emergent monopoles have included possible applications involving 'magnetricity' [20] and magnetothermal effects [21, 22], and there has been some success interpreting key material properties in the context of a gas of magnetic charges [23]. However, detailed measurements of existing spin ice materials at low temperatures have found large deviations between experiments and predictions of monopole theory [24], suggested to be a consequence of either cation-site inversion or oxygen deficiencies [25, 26]. As such, there is an active effort to identify and characterize new spin ice candidates.

In the past decade, several other spin-ice candidates with the 227 structure have been identified [27–30] and an entirely new area of artificial spin ice has emerged [31–33]. Here, we take a different approach and present evidence for a spin ice material with the spinel structure. Like the 227 magnets, spinels $A^{2+}B_2^{3+}X_4^{2-}$ have a magnetic sublattice of corner-sharing tetrahedra and have long been studied in the context of frustrated interactions [34–36]. The crystal field environment of spins on the B-site often drives a $< 111 >$ spin anisotropy, and in some materials ordered 2-in-2-out spin structures have been observed [37, 38]. The singular material $CdEr_2Se_4$ was briefly considered as a spin-ice candidate based on heat capacity and magnetization data [39], but the large absorption cross-section of cadmium prohibited further exploration of spin correlations using neutrons. To our knowledge, there has been no other work presenting evidence for spin ice behavior in a material with a spinel structure.

In this Letter, we report on the synthesis and characterization of the material $MgEr_2Se_4$, which might be thought of as a neutron-friendly analogue to $CdEr_2Se_4$. Using both X-ray and neutron diffraction, we confirm a nearly ideal spinel structure, and using inelastic neutron scattering, we fully determine the local crystal field environment at the Er^{3+} site. These spins are revealed to have largely Ising character; this finding is consistent with our magnetization, heat capacity and diffuse neutron scattering data, which strongly support the existence of a spin ice state at low temperatures. We argue that the spin ice behavior in $MgEr_2Se_4$, coupled with the absence of point defects, may make this material an ideal future testing ground for key monopole predictions.

Polycrystalline samples of $MgEr_2Se_4$ were prepared via a two-step solid state reaction, similar to the method described by Flahaut [40]. The precursors MgSe and Er_2Se_3 were prepared by the direct reaction of a stoichiometric amount of the elements at 650°C. Stoichiometric quantities of the two precursors were then combined, pelletized and reacted in vacuum at 1000°C for two days. The grinding and heating step was repeated once to ensure sample homogeneity. Structure and purity were confirmed with x-ray powder diffraction (XRD) using a PANalytical X'Pert^3 X-ray powder diffractometer at the Center for Nanophase Materials Sciences at Oak Ridge National Laboratory (ORNL), and followed with neutron powder diffraction (NPD) measurements

using the HB-2A powder diffractometer at ORNL's High Flux Isotope Reactor. NPD patterns were collected using a 3.6g sample and neutron wavelengths of $\lambda = 1.54$Å and $\lambda = 2.41$Å, with collimations of open-21'-12' and open-open-12' respectively at several temperatures. Structural refinements were performed using the FULLPROF [41] software suite. Inelastic neutron scattering (INS) was performed using the SEQUOIA [42] fine-resolution Fermi chopper spectrometer at ORNL's Spallation Neutron Source (SNS). Measurements were collected with incident energies $E_i = 30$meV and $E_i = 50$meV with the fine Fermi chopper spinning at frequencies of 300Hz and 360Hz respectively, and at temperatures $T \approx 4, 40$and150K. Magnetization and specific heat measurements were performed in the Seitz Materials Research Laboratory at Illinois. DC magnetization was measured with a Quantum Design MPMS 3, and specific heat was measured using a Quantum Design PPMS with a He_3 insert.

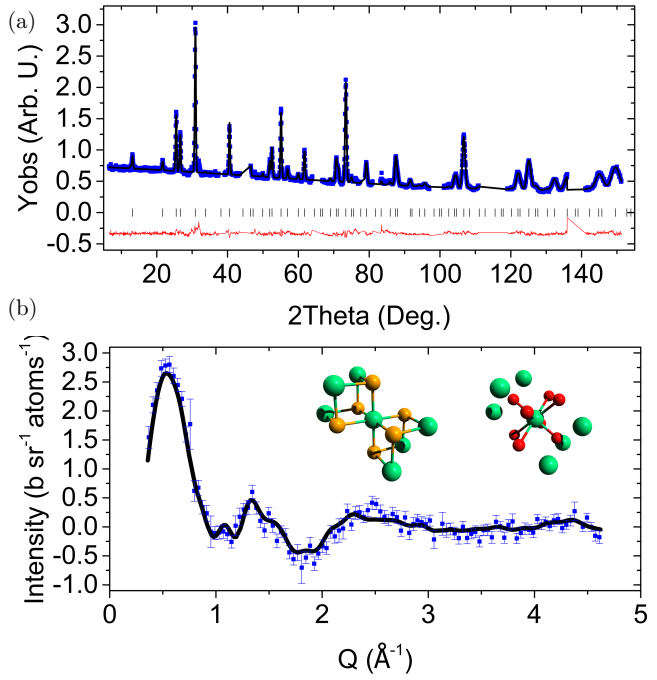

FIG. 1. (a) A representative NPD pattern in the non-magnetic state, with the corresponding refinement overlaid. (b) The difference between neutron diffraction patterns collected at $T \approx 470$mK and $T \approx 38$K. The solid lines in both panels correspond to fits described in the main text. (Inset) A schematic showing the local environment for the rare earth site in the spinels (left) and the pyrochlores (right).

Structural refinements of XRD data at room temperature and NPD data at $T \approx 38$K were performed separately and independently confirm that $MgEr_2Se_4$ is a cubic spinel with Er^{3+} ions comprising a pyrochlore sublattice of corner-sharing tetrahedra. As with other spinels, each Er^{3+} cation is found to sit in the center of a nearly-perfect Se octahedron, with a slight trigonal distortion along the local $\langle 111 \rangle$ directions. Fig. 1(a) shows a plot of the 38 K NPD pattern and illustrates the high quality of the structure refinements. Further NPD refinements at low temperature confirm that the structure of $MgEr_2Se_4$ does not change appreciably between $T \approx 300$K and 470mK, and no obvious sign of magnetic long-range order is observed. Instead, the emergence of appreciable magnetic diffuse scattering is found in the low temperature data, which is consistent with short-range spin ice correlations. The difference between the neutron diffraction patterns collected at $T \approx 470$mK and $T \approx 38$K is plotted in Fig. 1(b); we discuss this data in more detail below. Structural parameters resulting from the XRD and NPD refinements at high and low temperatures are given in the Supplementary Materials.

The x-ray and neutron cross-sections of Mg^{2+}, Er^{3+} and Se^{2-} are sufficiently distinct that the refinements should be extremely sensitive to common types of point disorder. The refinements allowed for the existence of both Mg-Er site inversion and Se deficiencies, and put a strict experimental upper bound of $< 1\%$ on either type of defect. As an additional check, we also performed "Lebail refinements" [43] of the patterns, in which each peak height is fit to the data independent of the calculated structure factor. As discussed in detail elsewhere [44], the nearly equal χ^2 resulting from Lebail analysis and our full refinements allow us to conclude that our material is *best* described by the ideal spinel structure, with a minimal density of *any* point defects, generally defined. The diffraction patterns did reveal a small amount ($\sim 5\%$) of an unidentified impurity phase, which does not alter our general conclusions in this work.

Magnetization and heat capacity data, shown in Fig. 2, are consistent with a spin ice Hamiltonian. Magnetization as a function of applied field, depicted in Fig. 2(a), shows that the moment of the sample saturates at a value near $4.3(2)\mu_B$. This moment size is equal to half the full moment of isolated Er^{3+} within our experimental error, which is consistent with Ising spins along the local $\langle 111 \rangle$ for a powder sample[45]. The temperature dependence shown in Fig. 2(b) is Curie-Weiss-like, with no sign of magnetic ordering down to $T = 2$K. Fits to a Curie-Weiss law with a constant offset yield a Weiss temperature of $\Theta = -0.37(1)K$, which is in line with measurements of other spin ice materials [5, 39].

Fig. 2(c) presents the low temperature heat capacity per Er atom, which reveals a peak near $T^* \approx 1$K and a residual entropy consistent with expectations for a spin ice. For the purpose of extracting residual entropy, the heat capacity was assumed to be the sum of four contributions arising from acoustic phonons, the CEF levels of the sample, a small impurity fraction, and magnetic correlations. The contribution from the phonons was captured using the Debye model, and the CEF contribution is taken to be that of an eight level system with the

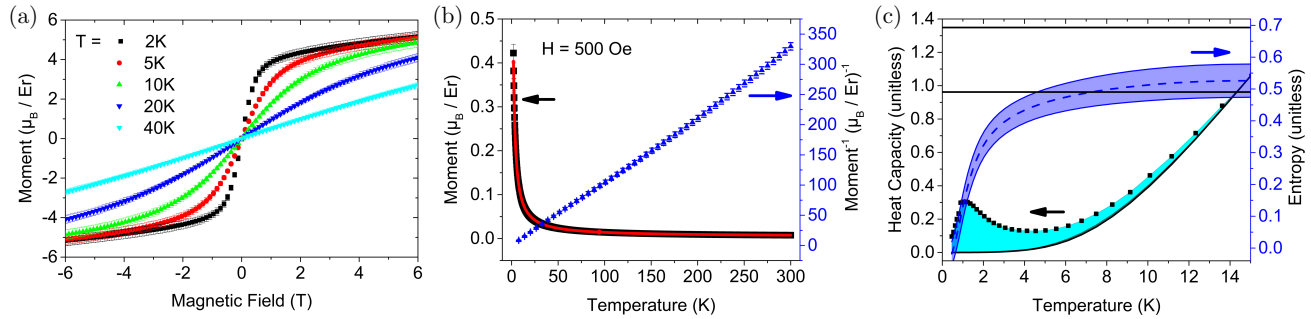

FIG. 2. Magnetization of $MgEr_2Se_4$ powders, measured as a function of (a) magnetic field and (b) temperature. Temperature data were collected in a field $H = 500$Oe (black squares) and fit to a Curie-Weiss function (solid curve). Inverse susceptibility (χ^{-1}) is plotted in the same panel (dashed line). (c) Dimensionless heat capacity (left axis) as a function of temperature. The black line represents the fitted CEF and phonon contribution, described in the main text, and the shaded region represents the magnetic contribution. The right axis shows the entropy loss inferred from the magnetic heat capacity, along with a solid line at $ln(2) - 1/2ln(3/2)$ showing the expectation for ice behavior. The experimental error in the entropy loss is represented by the shaded region.

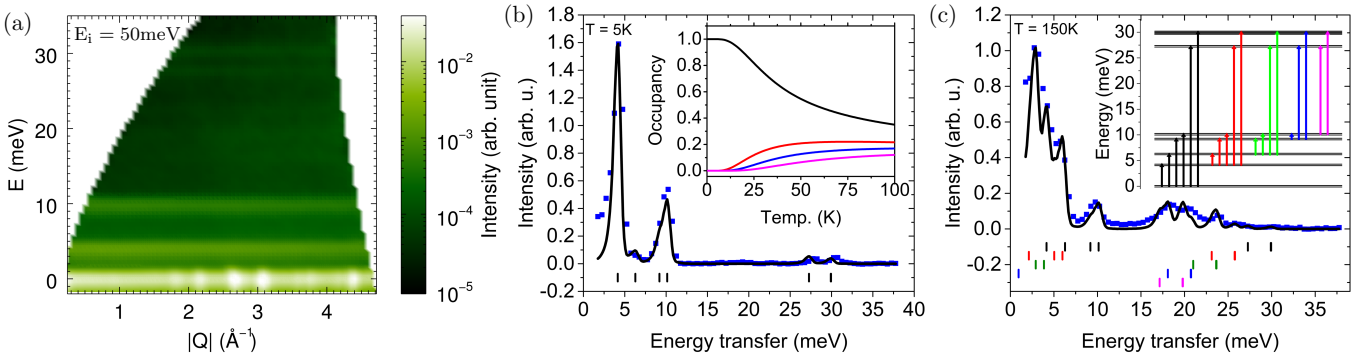

FIG. 3. Plots of representative inelastic neutron scattering measurements, taken with at $E_i = 50$meV. Shown are a contour plot of the scattering intensity as a function of energy transfer and momentum at $T \approx 5$K (a), along with $|Q| = [2, 2.5]$Å$^{-}1$ cuts at $T \approx 5$K (b) and $T \approx 150$K (c). Here, scattering intensity data is shown as solid squares and the curve of best fit as a solid black line. Peak positions are highlighted with tick marks below the data. The highest set of tick marks represent the set of transitions out of the ground state, while the next ones down indicate transitions out of the the 1st excited state, and so on. The panel (b) inset shows the CEF transitions that are allowed at $T \approx 150$K. The inset of panel (c) shows a plot of the occupancy of each CEF level as a function of temperature.

energy levels entirely determined by INS measurements discussed in detail below. The heat capacity contribution for the impurity phase was modeled with a Schottky anomaly set to 2.2meV, which is the energy scale identified from INS. The solid line in Fig. 2(c) represents contributions all non-magnetic components, inferred from fits of the data between $T = 7$K and $T = 25$K. The relative fraction of the impurity phase was varied by hand, and incorporated into the determination of uncertainty. The remaining heat capacity is assumed to be due entirely to the magnetic contribution. The magnetic entropy loss per Er (right axis, Fig. 2(c)) is distinctly less than ln(2) expected for a two level system, and in fact equal within error to the expected value $\ln(2) - 1/2\ln(3/2)$ for a spin ice system [4, 14]. The shaded region in this plot represents the experimental uncertainty in this entropy estimate, which accounts for measurement errors and the tolerances of the fitting procedure.

Further support for the conclusion of spin ice comes from both elastic and inelastic neutron scattering data. As noted above, NPD shows the onset of significant magnetic diffuse scattering at low temperature, as seen in other ice materials [30]. The background of the 38K NPD pattern is an excellent fit to the form factor squared of Er^{3+} plus a constant, confirming that the spins at $T \approx 38$K are essentially disordered. We thus plot in Fig. 1(b) the difference between the $T = 470$mK and 38K data, which effectively isolates the short-range magnetic correlations. Specifically, this plot corresponds to the quantity $\left(S^2(Q) - 1\right) \times f^2(Q)$, where $S(Q)$ is the structure factor and $f(Q)$ is the magnetic form factor of Er^{3+}. The solid curve corresponds to the best fit result-

ing from Reverse Monte Carlo (RMC) analysis performed using the software SPINVERT [46]. This analysis only assumes that the spins are Ising and point along the local ⟨111⟩ directions; the system size for the simulation was a 6×6×6 unit cell. Eight separate simulations were combined together to improve statistics. The resultant fits describe the data extremely well, and show that a majority (57(1)%) of the tetrahedra are in the 2-in-2-out configuration at 470mK, with this value decreasing slightly to 56(1)% at 1.5K and 48(1)% at 4K. Note that these values represent only a lower bound as the stochastic nature of the RMC fits will be the most disordered compatible with the data[30]. These values should be compared to the expectation of 37.5% 2-in-2-out tetrahedra for a random spin configuration.

Finally, and crucially, INS data allowed us to directly measure the CEF levels of the Er^{3+} ions and from this data we determined that the Er^{3+} spins have a strong Ising nature. In Fig. 3, we show representative INS data sets collected using various incident neutron energies E_i and sample temperatures, along with the calculated scattering intensity for our fitted model of the CEF levels. Color contour plots confirm the existence of multiple dispersionless modes, which we associate with local CEF excitations. To determine the exact level scheme, constant $Q = [2, 2.5]\text{Å}^{-1}$ ($Q = [1.5, 2]\text{Å}^{-1}$ for $\text{E}_\text{i} = 30\text{meV}$) cuts were made from the INS data and fit using a Monte Carlo method written for this purpose and detailed in the Supplementary Materials. Data was collected at $T \approx 5K$ to measure transitions out of the ground state doublet. Additional data was collected at higher temperatures to thermally-populate higher energy levels and therefore allow for the exploration of a greater number of inter-level transitions. The insets in Fig. 3 (b) and (c) pictorially represent the 12 distinct CEF transitions that we observed by this method.

Fits began with an initial guess calculated using a point charge model [47], with subsequent refinements of the potential to match the data. The model Hamiltonian was of the form,

$$H = \sum_{nm} B_n^m O_n^m \tag{1}$$

where O_n^m are the Stevens' operator equivalents to the spherical harmonics [48] and B_n^m are the crystal field parameters. Previously published values were used for the radius of the orbitals [49] and the shielding parameters [50]. For the potential calculation we included atoms as far away as $d = 11.5$ Å. This proved necessary, as the nearest neighbor Se atoms are in an almost perfect octahedral configuration and we unexpectedly found that the trigonal contribution to the CEF came primarily from neighboring Er^{3+} instead. This finding is in sharp contrast to the rare earth pyrochlores, such as $RE_2Ti_2O_7$, where the main contribution to the CEF is from the nearest neighbor O^{2-} atoms [26]. The CEF levels and electron wavefunctions were calculated with the quantization axis along the local ⟨111⟩ direction, and from the symmetry of the potential we only found the coefficients $B_2^0, B_4^0, B_4^3, B_6^0, B_6^3, B_6^6$ to be non-zero.

The calculation resuults in a set of intensities and energies for each peak, which were convoluted with the peak shape and width taken from the elastic line, and the resulting best fits of the data ae represented by the solid curves in Fig. 3. Convergence was reached with CEF parameters $B_2^0 = 1.4919\times10^{-24}, B_4^0 = 6.4296\times10^{-26}, B_4^3 = 8.4074\times10^{-26}, B_6^0 = -5.80027\times10^{-28}, B_6^3 = 4.6300\times10^{-28}$and, $B_6^6 = -3.6902\times10^{-28}$. These values led to a quantitative determination of the various crystal field levels in terms of $|J_z\rangle$ eigenstates, as detailed in the Supplemental Materials. The local ground state wavefunction of the Er^{3+} was determined to be $\psi_0 = \pm0.920\,|\pm15/2\rangle + 0.355\,|\pm9/2\rangle \pm 0.150\,|\pm3/2\rangle - 0.075\,|\mp3/2\rangle$, which yields an Er^{3+} moment of $g\mu_B\,\langle\psi_0|\,J_\alpha\,|psi_0\rangle = 8.324\mu_B$. The ground state wavefunction is a doublet with a large $|\pm15/2\rangle$ component which implies that the spins have a strong Ising character, although this is somewhat reduced as compared to $Dy_2Ti_2O_7$ and $Ho_2Ti_2O_7$ [51–53]. Additionally, the first excited level is not until $E_1 \approx 4.155$meV, which essentially eliminates the thermal occupation of excited states for temperatures $T < 10K$ (see the inset in Fig. 3(c)).

Altogether, the collective data on $MgEr_2Se_4$ leave little doubt that it hosts spin ice correlations at low temperatures. Diffraction confirms that Er^{3+} spins lie on a pyrochlore sublattice of corner-sharing tetrahedra, and direct measurements of the local crystal field environment show the near-Ising character of these spins at low temperatures. It is no surprise then that both short-range correlations from NPD and the residual entropy from heat capacity show ice signatures. To our knowledge, this is the first such material with a spinel structure wherein the spin correlations have been explored in such detail. While the expansion of spin ice physics to a new family of materials is interesting in its own right, we mention two other aspects of this development which are particularly exciting. Firstly, there is a demonstrably low level of cation site disorder or anion off-stoichiometry in this material, despite both of these effects being dominant sources of disorder in other pyrochlore and spinel systems. We suggest that this observation is no accident. The low level of selenium defects is consistent with the low synthesis temperature of this compound, as compared to oxides, and the reaction of the material in a selenium gas environment. The low level of cation inversion is consistent with the larger atomic radius of Er^{3+} compared with Mg^{2+}, which then gives the Er^{3+} the natural tendency to reside on the spinel B-site, where there is more room. As discussed at the beginning of this paper, these properties may then make $MgEr_2Se_4$ a natural testing ground for monopole physics. Secondly, we note the great flexibility of the spinel structure, which allows

for a wide range of cations to occupy both the A and B sublattices and a number of different chalcogenides to reside on the anion sublattice. We have already identified a number of analogous materials in this family with different rare earth cations, and the confirmation of spin ice behavior in $MgEr_2Se_4$ may portend opening up a new class of novel magnetic spinels.

We acknowledge useful discussions with P. Schiffer and G. Sala. The portion of this work performed at the University of Illinois was sponsored by the U.S. Department of Energy, Office of Science under grant number of de-sc0012368. Neutron scattering work was sponsored by the National Science Foundation, under grant number DMR-1455264-CAR. D.R. further acknowledges the partial support of by the U.S. D.O.E., Office of Science, Office of Workforce Development for Teachers and Scientists, Office of Science Graduate Student Research (SCGSR) program. The SCGSR program is administered by the Oak Ridge Institute for Science and Education for the DOE under contract number DE-AC05-06OR23100. Portions of this research was conducted at the Center for Nanophase Materials Sciences, at the High Flux Isotope Reactor and at the Spallation Neutron Source, each DOE Office of Science User Facilities operated by the Oak Ridge National Laboratory.

* gmacdoug@illinois.edu

[1] J. E. Greedan, Journal of Alloys and Compounds **408**, 444 (2006).
[2] J. S. Gardner, M. J. P. Gingras, and J. E. Greedan, Rev. Mod. Phys. **82**, 53 (2010).
[3] M. Harris, S. Bramwell, D. McMorrow, T. Zeiske, and K. Godfrey, Physical Review Letters **79**, 2554 (1997).
[4] A. P. Ramirez, A. Hayashi, R. Cava, R. Siddharthan, and B. Shastry, Nature **399**, 333 (1999).
[5] S. T. Bramwell and M. J. Gingras, Science **294**, 1495 (2001).
[6] R. Applegate, N. R. Hayre, R. R. P. Singh, T. Lin, A. G. R. Day, and M. J. P. Gingras, Phys. Rev. Lett. **109**, 097205 (2012).
[7] K. A. Ross, L. Savary, B. D. Gaulin, and L. Balents, Phys. Rev. X **1**, 021002 (2011).
[8] L. Pan, S. K. Kim, A. Ghosh, C. M. Morris, K. A. Ross, E. Kermarrec, B. D. Gaulin, S. Koohpayeh, O. Tchernyshyov, and N. Armitage, Nature communications **5** (2014).
[9] J. Gardner, S. Dunsiger, B. Gaulin, M. Gingras, J. Greedan, R. Kiefl, M. Lumsden, W. MacFarlane, N. Raju, J. Sonier, *et al.*, Physical review letters **82**, 1012 (1999).
[10] J. S. Gardner, B. D. Gaulin, A. J. Berlinsky, P. Waldron, S. R. Dunsiger, N. P. Raju, and J. E. Greedan, Phys. Rev. B **64**, 224416 (2001).
[11] Villain, J., Bidaux, R., Carton, J.-P., and Conte, R., J. Phys. France **41**, 1263 (1980).
[12] J. Champion, M. Harris, P. Holdsworth, A. Wills, G. Balakrishnan, S. Bramwell, E. Čižmár, T. Fennell, J. Gardner, J. Lago, *et al.*, Physical Review B **68**, 020401 (2003).
[13] B. C. den Hertog and M. J. P. Gingras, Phys. Rev. Lett. **84**, 3430 (2000).
[14] Pauling Linus, Journal of the American Chemical Society **57**, 2680 (1935), doi: 10.1021/ja01315a102.
[15] T. Fennell, S. Bramwell, D. McMorrow, P. Manuel, and A. Wildes, Nature Physics **3**, 566 (2007).
[16] T. Fennell, P. Deen, A. Wildes, K. Schmalzl, D. Prabhakaran, A. Boothroyd, R. Aldus, D. McMorrow, and S. Bramwell, Science **326**, 415 (2009).
[17] C. Castelnovo, R. Moessner, and S. L. Sondhi, Nature **451**, 42 (2008).
[18] D. J. P. Morris, D. Tennant, S. Grigera, B. Klemke, C. Castelnovo, R. Moessner, C. Czternasty, M. Meissner, K. Rule, J.-U. Hoffmann, *et al.*, Science **326**, 411 (2009).
[19] H. Kadowaki, N. Doi, Y. Aoki, Y. Tabata, T. J. Sato, J. W. Lynn, K. Matsuhira, and Z. Hiroi, Journal of the Physical Society of Japan **78**, 103706 (2009).
[20] S. Bramwell, S. Giblin, S. Calder, R. Aldus, D. Prabhakaran, and T. Fennell, Nature **461**, 956 (2009).
[21] M. J. Jackson, E. Lhotel, S. Giblin, S. Bramwell, D. Prabhakaran, K. Matsuhira, Z. Hiroi, Q. Yu, and C. Paulsen, Physical Review B **90**, 064427 (2014).
[22] C. Paulsen, M. J. Jackson, E. Lhotel, B. Canals, D. Prabhakaran, K. Matsuhira, S. Giblin, and S. Bramwell, Nature Physics **10**, 135 (2014).
[23] C. Castelnovo, R. Moessner, and S. L. Sondhi, Phys. Rev. B **84**, 144435 (2011).
[24] L. D. Jaubert and P. C. Holdsworth, Journal of Physics: Condensed Matter **23**, 164222 (2011).
[25] Revell H. M., Yaraskavitch L. R., Mason J. D., Ross K. A., Noad H. M. L., Dabkowska H. A., Gaulin B. D., Henelius P., and Kycia J. B., Nat Phys **9**, 34 (2013), 10.1038/nphys2466.
[26] G. Sala, M. J. Gutmann, D. Prabhakaran, D. Pomaranski, C. Mitchelitis, J. B. Kycia, D. G. Porter, C. Castelnovo, and J. P. Goff, Nat Mater **13**, 488 (2014), article.
[27] X. Ke, B. Ueland, D. West, M. Dahlberg, R. Cava, and P. Schiffer, Physical Review B **76**, 214413 (2007).
[28] X. Ke, M. Dahlberg, E. Morosan, J. Fleitman, R. Cava, and P. Schiffer, Physical Review B **78**, 104411 (2008).
[29] H. Zhou, S. Bramwell, J. Cheng, C. Wiebe, G. Li, L. Balicas, J. Bloxsom, H. Silverstein, J. Zhou, J. Goodenough, *et al.*, Nature communications **2**, 478 (2011).
[30] A. M. Hallas, J. A. M. Paddison, H. J. Silverstein, A. L. Goodwin, J. R. Stewart, A. R. Wildes, J. G. Cheng, J. S. Zhou, J. B. Goodenough, E. S. Choi, G. Ehlers, J. S. Gardner, C. R. Wiebe, and H. D. Zhou, Phys. Rev. B **86**, 134431 (2012).
[31] I. Gilbert, C. Nisoli, and P. Schiffer, Physics Today **69**, 54 (2016).
[32] Y.-L. Wang, Z.-L. Xiao, A. Snezhko, J. Xu, L. E. Ocola, R. Divan, J. E. Pearson, G. W. Crabtree, and W.-K. Kwok, Science **352**, 962 (2016).
[33] E. Iacocca, S. Gliga, R. L. Stamps, and O. Heinonen, Phys. Rev. B **93**, 134420 (2016).
[34] S.-H. Lee, H. Takagi, D. Louca, M. Matsuda, S. Ji, H. Ueda, Y. Ueda, T. Katsufuji, J.-H. Chung, S. Park, *et al.*, Journal of the Physical Society of Japan **79**, 011004 (2010).
[35] H. Takagi and S. Niitaka, in *Introduction to Frustrated Magnetism*, Vol. 164, edited by C. M. P. M. F. Lacroix (Springer-Verlag Berlin Heidelberg, 2011) 1st ed.,

Chap. 7, pp. 155–175.
[36] P. G. Radaelli, New Journal of Physics **7**, 53 (2005).
[37] G. MacDougall, V. Garlea, A. Aczel, H. Zhou, and S. Nagler, Physical Review B **86**, 060414 (2012).
[38] G. J. MacDougall, I. Brodsky, A. A. Aczel, V. O. Garlea, G. E. Granroth, A. D. Christianson, T. Hong, H. D. Zhou, and S. E. Nagler, Phys. Rev. B **89**, 224404 (2014).
[39] J. Lago, I. Živković, B. Malkin, J. Rodriguez Fernandez, P. Ghigna, P. Dalmas de Réotier, A. Yaouanc, and T. Rojo, Physical review letters **104**, 247203 (2010).
[40] J. Flahaut, M. Guittard, M. Patrie, M. P. Pardo, S. M. Golabi, and L. Domange, Acta Crystallographica **19**, 14 (1965).
[41] J. Rodríguez-Carvajal, Physica B: Condensed Matter **192**, 55 (1993).
[42] G. Granroth, D. Vandergriff, and S. Nagler, Physica B: Condensed Matter **385–386, Part 2**, 1104 (2006), proceedings of the Eighth International Conference on Neutron Scattering.
[43] A. Le Bail, H. Duroy, and J. Fourquet, Materials Research Bulletin **23**, 447 (1988).
[44] B. H. Toby, Powder diffraction **21**, 67 (2006).
[45] S. Bramwell, M. Field, M. Harris, and I. Parkin, Journal of Physics: Condensed Matter **12**, 483 (2000).
[46] J. A. Paddison, J. R. Stewart, and A. L. Goodwin, Journal of Physics: Condensed Matter **25**, 454220 (2013).
[47] M. Hutchings, in , Solid State Physics, Vol. 16, edited by F. Seitz and D. Turnbull (Academic Press, 1964) pp. 227–273.
[48] K. Stevens, Proceedings of the Physical Society. Section A **65**, 209 (1952).
[49] J. Forstreuter, L. Steinbeck, M. Richter, and H. Eschrig, Phys. Rev. B **55**, 9415 (1997).
[50] R. M. Sternheimer, M. Blume, and R. F. Peierls, Phys. Rev. **173**, 376 (1968).
[51] M. Ruminy, E. Pomjakushina, K. Iida, K. Kamazawa, D. Adroja, U. Stuhr, and T. Fennell, Physical Review B **94**, 024430 (2016).
[52] S. Rosenkranz, A. Ramirez, A. Hayashi, R. Cava, R. Siddharthan, and B. Shastry, Journal of Applied Physics **87**, 5914 (2000).
[53] A. Bertin, Y. Chapuis, P. D. de Réotier, and A. Yaouanc, Journal of Physics: Condensed Matter **24**, 256003 (2012).

Supplementary information

Structural parameters

The results of both NPD and XRD refinements is shown in table I. Fits of each dataset were performed with FULLPROF, and the fits independantly confirmed the structure and purity of the material. To check for point defects we allowed for the Se occupancy to vary, and separately allowed for Mg and Er exchange. As and additional check we performed both standard and "Lebail" refinements, where the peak heights are varied independantly of any structure factor. Since any point defects would affect the peak height, a match in the quality of fit between "Lebail" and standard refinements shows that a point-defect-free model decribes the data best.

Additional INS plots

Shown in Fig. 4 are the data and fits for INS data taken at $E_i = 30$mev which were not included in the main text. These plots show the level of detail captured by our fits of the CEF scheme, and that at both energies the data is very well described by the fit.

$MgEr_2Se_4$ lattice parameters space group $Fd\bar{3}m$			
	XRD 300K	NPD 38K	NPD 470mK
a	11.5207(14)	11.4999(42)	11.5048(81)
χ^2	10.41	6.39	8.63
χ^2 Lebail	11.40	6.83	9.53
Se deficiency (%)	0.00(70)	0.00(98)	0.0(1.2)
Site inversion (%)	0.00(47)	0.0(3.7)	0.0(4.5)

$MgEr_2Se_4$ atom positions				
	x	y	z	$B_{iso}(Å^2)$
Mg	0.375	0.375	0.375	0.2(1)
Er	0.000	0.000	0.000	0.39(5)
Se	0.2456(9)	0.2456(9)	0.2456(9)	0.40(3)

TABLE I. Structural parameters obtained from the XRD and NPD refinements of $MgEr_2Se_4$ data. The structural parameters in the lower part of the table are from the 38K NPD refinement.

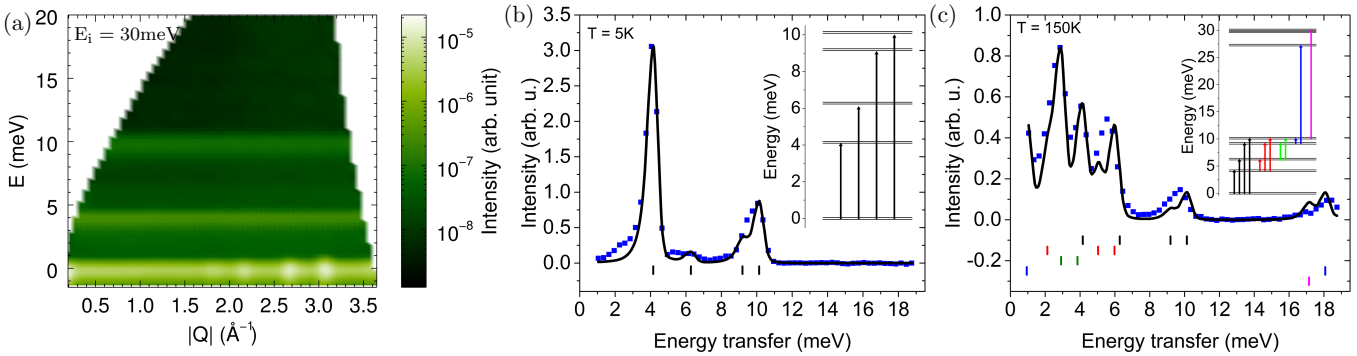

FIG. 4. Plots of the INS data taken at $E_i = 30$mev. Shown are a contour plot of the scattering intensity as a function of energy transfer and momentum at $T \approx 5$K (a), along with $|Q| = [1.5, 2]$Å$^{-}1$ cuts at $T \approx 5$K (b) and $T \approx 150$K (c). Here, scattering intensity data is shown as solid squares and the curve of best fit as a solid black line. Peak positions are highlighted with tick marks below the data. The highest set of tick marks represent the set of transitions out of the ground state, while the next ones down indicate transitions out of the the 1st excited state, and so on. The panel (b) and (c) insets show the availiable transitions at $T = 5$and150K respectively.

INS fitting method and results

The resulting wavefunctions for all CEF levels is shown in table II. The code for fitting the INS data to the CEF model was written in MATLAB. The assumptions for the refinement are as follows: the CEF levels are thermally populated according to the partition function $Z = \sum_n \exp(-\beta E_n)$, where E_n is the energy of the n^{th} CEF level. Excitation energies are determined by diagonalizing the Hamiltonian

$$H = \sum_{nm} B_n^m O_n^m \tag{2}$$

and taking the difference between every pair of eigenvalues. In order to isolate the unique solution where the wavefunctions are maximally parallel/antiparallel to the $\langle 111 \rangle$ directions, a small field of 10^{-7} T is added to the potential; we note that this field is too small to change the energy of the calculated CEF levels. Peak intensities are given by $p_n \langle \psi_n | J_\alpha | \psi_m \rangle^2$ where p_n is the probability of an Er^{3+} ion being in the ψ_n state, and $J_\alpha = J_- + J_+ + J_z$. The energy width and peak shape of the excitations are derived from the incoherent elastic scattering. The fitting was done using a Monte Carlo refinement method that explores the six dimensional phase space of the six non-zero B_n^m coefficients. The variation within this phase space was done by projecting random vectors in the phase space and then finding the least squares minima of the simulated pattern along those vectors. The overall minimum is then taken as the next starting point, and the process is repeated until convergence. The program was initially run with the lowest-lying CEF excitation fixed to $E = 4.1$meV, thereby limiting the search to vectors in the five dimensional manifold that satisfied this condition. After initial convergence, this condition was relaxed. To check against false minima, the program was run eight separate times.

			$MgEr_2Se_4$ crystal field levels
n	δE (meV)	Rel. Int.	Ψ_n
0	0	-	$\pm 0.920 \lvert \pm 15/2 \rangle + 0.355 \lvert \pm 9/2 \rangle \pm 0.150 \lvert \pm 3/2 \rangle - 0.075 \lvert \mp 3/2 \rangle$
1	4.155	1	$-0.739 \lvert \pm 13/2 \rangle \mp 0.484 \lvert \pm 7/2 \rangle - 0.432 \lvert \pm 1/2 \rangle \pm 0.175 \lvert \mp 5/2 \rangle - 0.047 \lvert \mp 11/2 \rangle$
2	6.279	0.0517	$\mp 0.473 \lvert \pm 13/2 \rangle - 0.070 \lvert \pm 7/2 \rangle \pm 0.873 \lvert \pm 1/2 \rangle \mp 0.079 \lvert \mp 11/2 \rangle$
3	9.193	0.0862	$\mp 0.256 \lvert \pm 15/2 \rangle + 0.249 \lvert \pm 9/2 \rangle \pm 0.921 \lvert \pm 3/2 \rangle - 0.134 \lvert \mp 3/2 \rangle - 0.071 \lvert \mp 15/2 \rangle$
4	10.133	0.2846	$\pm 0.661 \lvert \pm 11/2 \rangle + 0.727 \lvert \pm 5/2 \rangle \mp 0.078 \lvert \mp 1/2 \rangle \mp 0.166 \lvert \mp 13/2 \rangle$
5	27.273	0.0329	$\pm 0.693 \lvert \pm 11/2 \rangle - 0.566 \lvert \pm 5/2 \rangle \pm 0.186 \lvert \mp 1/2 \rangle + 0.347 \lvert \mp 7/2 \rangle \pm 0.209 \lvert \mp 13/2 \rangle$
6	29.91	0.0188	$+0.288 \lvert \pm 15/2 \rangle \mp 0.900 \lvert \pm 9/2 \rangle + 0.309 \lvert \pm 3/2 \rangle \mp 0.105 \lvert \mp 3/2 \rangle$
7	29.945	0.0055	$+0.399 \lvert \pm 13/2 \rangle \mp 0.800 \lvert \pm 7/2 \rangle + 0.105 \lvert \pm 1/2 \rangle \mp 0.342 \lvert \mp 5/2 \rangle - 0.270 \lvert \mp 11/2 \rangle$

TABLE II. Table showing the full CEF scheme of $MgEr_2Se_4$ as calculated from the best fit to the data. Table displayes in order the CEF energy levels, relative neutron scattering intensity at 0K, and wavefunctions, disregarding components with factors smaller than 0.05.